Energy Extension in Three-Dimensional Atomic Imaging by Electron-Emission Holography

S. Y. Tong, Hua Li, and H. Huang

Department of Physics and Laboratory for Surface Studies, University of Wisconsin-Milwaukee, Milwaukee, Wisconsin 53201

(Received 13 December 1990)

A method is introduced joining together forward-scattering diffraction data taken in a small angular window at different photoelectron energies. This method extends the usable range in phase space for three-dimensional image reconstruction. Examples based on theoretical simulations demonstrate that a spatial resolution of ≤ 1 Å is achievable. We also show that using a small angular window in the backscattering geometry eliminates splittings in the reconstructed image.

PACS numbers: 68.35.Bs, 68.55.−a

When forming three-dimensional atomic images from electron-emission holography [1–5], there are two objectives: (i) that the images are formed at the correct atomic positions and (ii) that the full width at half magnitude (FWHM) of the image is as small as possible. The FWHM defines the ability of a "microscope" to produce distinct images of two closely spaced objects. The best resolution of the current state-of-the-art conventional electron microscope is 2–3 Å. In electron-emission holography, a limiting factor is the small angular range of usable data available in $\mathbf{k}$ space for image reconstruction. In the forward-scattering geometry, most systems have multiple focusing directions [6]. In such systems, the diffraction fringes in an angular cone around each focusing direction are dominated by the scattering of atoms situated along that particular direction [7,8]. Therefore, the relevant interference fringes for image reconstruction for atoms in a particular direction are limited to within the effective angular cone Ω_c, which is much smaller than the full $\Omega_{2\pi}$ opening [7,9]. In the backscattering geometry, deep cusps in the scattering factor of many materials limit the effective angular range to a small cone in the reconstruction process. As we shall see later, these cusps cause image peaks to be split [10]. Since the diffraction limit for resolution is $\Delta r_\alpha = 2.4\pi/\Delta k_\alpha$, where α is a Cartesian-coordinate index, the small range of applicable $\Delta\mathbf{k}$ limits the achievable spatial resolution.

In this paper, we show how this serious limitation of the technique can be lifted through the use of multiple energies in which diffraction data in a given angular cone taken at different emission energies are connected to form an extended range. When used in conjunction with a variable energy source (e.g., a synchrotron radiation center or Kikuchi electrons), this method can reach a spatial resolution of less than 1 Å in the direction of the emitter scatterer. This direction has a worse resolution (≥ 2.5 Å) in single-energy image reconstructions [2–6, 9,10].

For the purpose of image reconstruction, we use x-ray-photoemission-spectroscopy (XPS) diffraction spectra calculated by the multiple-scattering slab method in which the crystal is rotated while the directions of photon incidence and electron exit are held fixed. This collection mode eliminates the anisotropy in the unscattered wave from any initial atomic core level [9]. Since the reference wave in this collection mode is continuously varying, we introduce an image reconstruction method based directly on three-dimensional Fourier transformation instead of the Helmholtz-Kirchhoff integral used by Barton [2]. At each energy E_n, we can write

$$\phi_n(\mathbf{R}) = |T_n(\mathbf{R})|\,, \tag{1}$$

$$\phi_n(\mathbf{R}) = \left| \int \chi(k_n\hat{\mathbf{k}})\delta(k-k_n)e^{ik_n\hat{\mathbf{k}}\cdot\mathbf{R}}d^3k \right|, \tag{2}$$

where $k_n = [(2m/\hbar^2)E_n]^{1/2}$ and $\chi(k_n\hat{\mathbf{k}}) = [I(k_n\hat{\mathbf{k}}) - A]/A$. Here, $I(k_n\hat{\mathbf{k}})$ is a measured or calculated XPS intensity at $k = k_n$, and A is its angle-averaged value. Using $d^3k = k^2 dk\, d\Omega$ to integrate out the δ function in Eq. (2), we obtain

$$T_n(\mathbf{R}) = \int \chi(k_n\hat{\mathbf{k}})e^{ik_n\hat{\mathbf{k}}\cdot\mathbf{R}}k_n^2 d\Omega\,. \tag{3}$$

Energy extension involves summing the complex function $T_n(\mathbf{R})$ over a discrete set of energies with a particular phase factor [9–11]. By considering N energy points, in ascending order of magnitude, with wave numbers $k_1, \ldots, k_N$, a generalized energy-extended image function can be written as

$$\Phi_{R_i}(\mathbf{R}) = \mathcal{D}\left| \sum_{n=1}^{N} e^{-ik_nR_i}T_n(\mathbf{R}) \right|, \tag{4}$$

where $\mathcal{D} = (k_N - k_1)/(N-1)$ defines a mean wave-number interval and R_i is a scalar which defines the phase that joins together single-energy Fourier transforms $T_n(\mathbf{R})$. By substituting $T_n(\mathbf{R})$ from Eq. (3) and using $k_n^2 d\Omega = dk_\parallel^n/\cos\theta$, we obtain

$$\Phi_{R_i}(\mathbf{R}) = \mathcal{D}\left| \sum_{n=1}^{N} \int \frac{\chi(k_n\hat{\mathbf{k}})e^{-ik_nR_i}e^{ik_n\hat{\mathbf{k}}\cdot\mathbf{R}}}{\cos\theta} dk_{n,x}dk_{n,y} \right|. \tag{5}$$

In the forward-scattering geometry, the first step is to determine $\mathbf{R}_\alpha$, the atomic position of the scatterer [9,10]. The orientation (i.e., θ,ϕ) of $\mathbf{R}_\alpha$ can be determined from the αth focusing direction in $\mathbf{k}$ space. To determine the magnitude, we substitute $R_i = R$ in Eq. (5) and evaluate $\Phi_R^\alpha(R)$ along this focusing direction. The position of the maximum along this line determines the bond distance R_α. The justification of this step is that at $R_i = R_\alpha$, the

phase factor e^{-ikR_i} exactly cancels the conjugate phase in $\chi(k_n\hat{\mathbf{k}})$, thereby leaving only a plane-wave phase $e^{ik_n\hat{\mathbf{k}}\cdot\hat{\mathbf{R}}_a}$ for all the energies. Therefore, after performing the Fourier transformation by Eq. (5), the contribution from each energy coherently cumulates at the image point $\Phi_{R_a}(\mathbf{R}_a)$, giving the desired result. Also, since only the single-scattering term in $\chi(k_n\hat{\mathbf{k}})$ has this conjugate phase, the sum in Eq. (5) reinforces the single-scattering contribution to the image and reduces (by phase cancellation) the multiple-scattering contributions [11]. After R_a is determined, we form the corresponding image by substituting $R_i = R_a$ in Eq. (5) and obtain [9,10]

$$\Phi_{R_a}(\mathbf{R}) = \mathcal{D}\left| \sum_{n=1}^{N} \int \frac{\chi(k_n\hat{\mathbf{k}})e^{-ik_nR_a}e^{ik_n\hat{\mathbf{k}}\cdot\mathbf{R}}}{p_a(k_n\hat{\mathbf{k}})\cos\theta} dk_{n,x}dk_{n,y} \right|, \tag{6}$$

where $p_a(k_n\hat{\mathbf{k}})$ is a phase-shift correction function defined in earlier works [5,9]. We shall show elsewhere that Eq. (6) corresponds to cutting across the high-intensity contours of $\Phi_{R_i}(R)$ at a particularly narrow cross section [6,10]. More importantly, this cut avoids the self-image artifacts near the origin [9,10,12,13]. The image, so formed, has a narrow FWHM and a low level of noise in the space between the emitter and the scatterer [6].

We now illustrate these ideas with a specific example: Si(111)$(\sqrt{3}\times\sqrt{3})R30°$-B. We first show the geometric structure of this system in Fig. 1. In this system, the B atoms occupy substitutional sites (i.e., the B_5 site) in the second layer [14–18]. The atomic images are reconstructed from calculated B(1s) XPS holograms, at photoelectron energies of 400, 600, and 800 eV. For the calculation, we use a multiple-scattering slab method [19,20] which uses the exact Green's-function structural propagators to evaluate the near-field (i.e., curved wave) scattering t matrices. Approximation schemes, such as the separable representation [21] or Taylor-series, magnetic-quantum-number expansion [22], etc., are not used. The photon's incident direction and the electron's exit angle are fixed at 70° apart while the crystal is rotated to generate the 2π hemispherical scan. The photon is p polarized and the $s \rightarrow p$ transition matrix element is calculated explicitly [23]. We demonstrate the multiple-energy image reconstruction procedure by forming the image of Si(3). We use $\chi(k_n\hat{\mathbf{k}})$ inside an angular cone whose half angle is $\theta_c = 45°$. The axis of this cone is pointed along the focusing direction of B-Si(3). Figure 2 shows the images of Si(3) reconstructed from single-energy diffraction patterns (top left, center, and right, respectively) while the image from joining the 400, 600, and 800 eV energies is shown in the bottom left panel. In the displays, crosses mark the origin and the correct atomic positions. We obtain a substantial improvement in the resolution with the elongation in the emitter-scatterer direction almost all gone. We also show the intensity variation of the image along the emitter-scatterer direction (i.e., $\theta = 62.9°$). The FWHM of the image from the individual 400-eV diffraction pattern is 2.2 Å (bottom right) and this value is reduced to 1.1 Å (bottom center) after energy extension; the noise level is also sharply reduced, especially at small R values.

In the backscattering geometry, using the phases $e^{\pm ik_nR}$ for the half planes $R_z > 0$ and $R_z \leq 0$, respectively, correspond to a line of 135° passing through the origin of $\Phi_{R_i}(R)$. We show elsewhere that this line cuts across the high-intensity contours of the images, self-images, and twin images at their narrowest cross sections [10].

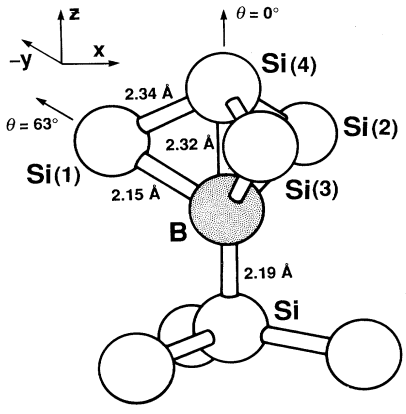

FIG. 1. Diagram of structure of Si(111)$(\sqrt{3}\times\sqrt{3})R30°$-B. The Si(3), Si(4), and B atoms lie in the y-z plane.

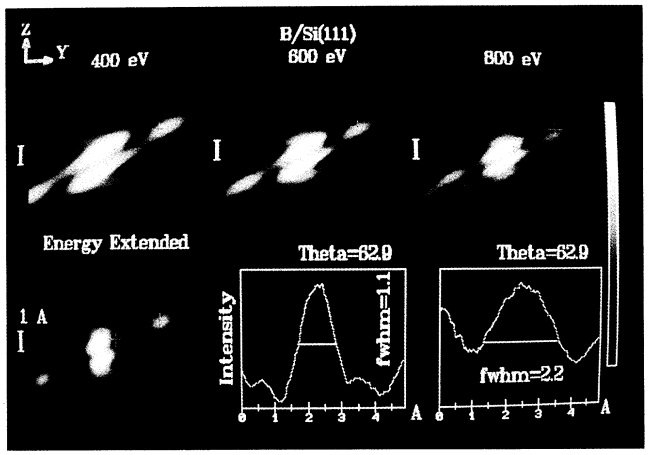

FIG. 2. Small-window $\theta_c = 45°$ image of Si(3) in the y-z plane; top left, center, and right show single-energy reconstructions; bottom left shows 3-energy combined reconstruction; crosses mark origin and correct atomic position. Bottom center and right show, respectively, intensity variation along the B-Si(3) internuclear direction for 3-energy combined and 400-eV reconstructions. The origin is at the B atomic center.

Substituting these phases in Eq. (5), we obtain, respectively,

$$\Phi(\mathbf{R})=\mathcal{D}\left|\sum_{n=1}^{N}\int\frac{\chi(k_n\hat{\mathbf{k}})e^{ik_nR}e^{ik_n\hat{\mathbf{k}}\cdot\mathbf{R}}}{\cos\theta}dk_{n,x}dk_{n,y}\right| \quad (R_z>0) \tag{7a}$$

and [11]

$$\Phi(\mathbf{R})=\mathcal{D}\left|\sum_{n=1}^{N}\int\frac{\chi(k_n\hat{\mathbf{k}})e^{-ik_nR}e^{ik_n\hat{\mathbf{k}}\cdot\mathbf{R}}}{\cos\theta}dk_{n,x}dk_{n,y}\right| \quad (R_z\leq 0)\,, \tag{7b}$$

where the $+z$ direction is normal to the surface and points from solid to vacuum.

The example we show in the backscattering geometry is for an ordered layer of Cu atoms occupying the four-fold-hollow site on Ni(001) with a Cu-Ni spacing of 1.8 Å. The energy-extension scheme uses 17 energies, from 60 to 681 eV with *equally spaced wave-number intervals*. This leads to a period of $L=10.7$ Å in $\Phi_{R_i}(R)$ [6,9]. The use of equally spaced wave numbers is critical to the multiple-energy image reconstruction scheme in the backscattering geometry [10]. We show in Fig. 3 the energy-extended images reconstructed from holograms calculated by the multiple-scattering slab method. The emission is from Cu($2p$) and the matrix elements $p\rightarrow s,d$ are explicitly evaluated [23]. The left-hand side shows a plane normal to the surface passing through the Cu emitter (marked by a cross) and two nearest-neighbor Ni atoms (marked by circles) as well as a next-nearest-neighbor Ni atom directly below the Cu atom (marked by a circle). The images of the two nearest Ni neighbors are 2.38 Å from the origin (correct distance is 2.52 Å; error is 0.14 Å). The image FWHM is 0.69 Å. The image of the next-nearest-neighbor Ni atom directly below the Cu atom is at 3.25 Å (correct distance is 3.56 Å; error is 0.31 Å). Since Eqs. (7a) and (7b) correspond to a line passing through the image and twin, the surface is a mirror plane and the twins appear in the $z>0$ half plane [10]. The right-hand side of Fig. 3 shows a cut parallel to the surface at 1.8 Å below the Cu plane. This plane passes through the first-layer Ni nuclei. The image reconstruction shows four nearest-neighbor Ni atoms, whose distance from the center is 2.12 Å (correct distance is 1.76 Å; error is 0.36 Å).

The nearest- and next-nearest-neighbor Ni images become split if we reduce the range to 60–286 eV. This is because in the 100–300-eV range, the backscattering factor $f(\pi-\theta)$ has deep cusps at which the magnitude of $|f(\pi-\theta)|$ almost vanishes. At these cusps, the phase of $f(\pi-\theta)$ goes through a near π resonance. The sharp cusps and π change in the phase of $f(\pi-\theta)$ cause the image peaks to become split [10].

We show in Fig. 4, left-hand side, the split Ni images; except for the reduced energy range which requires only nine energies to maintain the same period, all other conditions are identical to those of Fig. 3, left-hand side. The image of the nearest-neighbor Ni atom shows a doublet at 1.82 and 2.75 Å, respectively, compared to the correct spacing of 2.52 Å. The next-nearest-neighbor atom directly below the emitter shows a doublet at 2.60 and 3.71 Å, respectively, compared to the correct spacing of 3.56 Å. Since the image splitting is due to deep cusps in $f(\pi-\theta)$, we can remove this splitting by imposing a small window which limits $\chi(k_n\hat{\mathbf{k}})$ to the near π backscattering lobe in $f(\pi-\theta)$. We show in Fig. 4, right-hand side, the image constructed by introducing a small-window angular cone whose axis is at a polar angle of 136° from the positive abscissa direction. The half open-

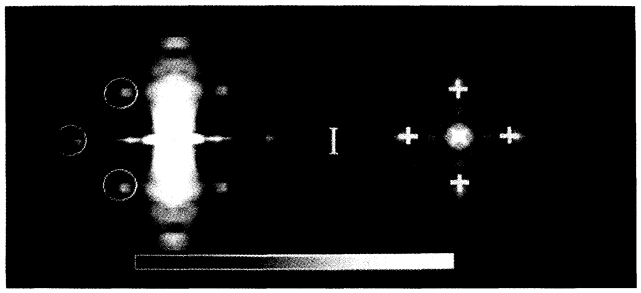

FIG. 3. Left: Full-window $\theta_c=90°$ image of Ni atoms (inside circles) in a plane normal to the surface, the cross marks the Cu emitter. The $+\hat{z}$ direction points from left to right and the twin images are mirrored on the right half. The energy range is 60–681 eV. Right: Plane parallel to the surface, crosses mark the correct atomic positions. The vertical bar indicates 1 Å.

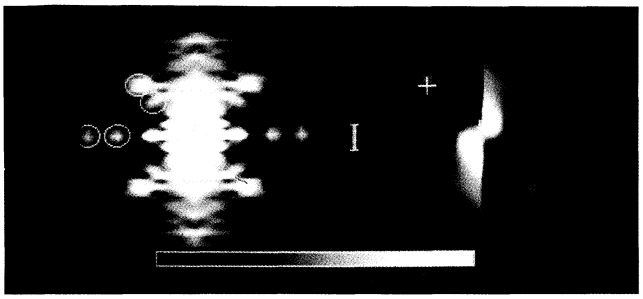

FIG. 4. Left: Full-window $\theta_c=90°$ Ni images using nine energies in the 60–286 eV range. Other conditions are the same as those in Fig. 3, left. The Ni images are split (marked by circles). Right: Small-window $\theta_c=45°$ image of nearest-neighbor Ni atom. Crosses mark the origin (emitter) and correct Ni atomic position. The vertical bar indicates 1 Å.

ing of the cone is $\theta_c = 45°$. We see from the figure that the nearest-neighbor Ni image is no longer split; the image forms at the cross which marks the correct atomic position. We can similarly remove the splitting in the image of the next-nearest-neighbor Ni atom directly below the Cu emitter: For this, we use a small angular cone of $\theta_c = 30°$ centered at 180° from the positive abscissa direction. The small-window image of this Ni atom is shown elsewhere [10].

A distinct feature of our method is the use of a small angular window Ω_c for image reconstruction. In the forward-scattering geometry, diffraction fringes within Ω_c are dominated by the scattering of a single atom or chain of atoms in the direction along the central axis of the cone. By joining together diffraction data taken at different energies in the same angular window Ω_c, we obtain an extended range of "exclusive" diffraction data due to atoms in a specific direction. We call this scheme the small-window energy-extension process (SWEEP). In the backscattering geometry, a full window is first used to locate the general areas of the images. If an image is split or the noise level around it is high, a small angular cone *centered along the particular emitter-image direction* is applied and SWEEP is carried out using $\chi(k_n\hat{\mathbf{k}})$ in that angular cone only. This process is repeated for images in other directions [10].

This work is supported by the National Science Foundation, Grant No. DMR-8805938. We acknowledge T. C. Zhao and C. M. Wei for valuable graphic assistance.

[1] A Szoeke, in *Short Wavelength Coherent Radiation: Generation and Applications,* edited by D. T. Attwood and J. Boker, AIP Conf. Proc. No. 147 (American Institute of Physics, New York, 1986).

[2] J. J. Barton, Phys. Rev. Lett. **61**, 1345 (1988).

[3] G. R. Harp, D. K. Saldin, and B. P. Tonner, Phys. Rev. Lett. **65**, 1012 (1990).

[4] C. M. Wei, T. C. Zhao, and S. Y. Tong, Phys. Rev. Lett. **65**, 2278 (1990).

[5] S. Y. Tong, C. M. Wei, T. C. Zhao, H. Huang, and Hua Li, Phys. Rev. Lett. **66**, 60 (1991).

[6] H. Huang, Hua Li, and S. Y. Tong, Phys. Rev. B **44**, 3240 (1991).

[7] H. C. Poon and S. Y. Tong, Phys. Rev. B **30**, 6211 (1984); S. Y. Tong, H. C. Poon, and D. R. Snider, Phys. Rev. B **32**, 2096 (1985); M. L. Xu and M. A. Van Hove, Surf. Sci. **207**, 215 (1989).

[8] W. F. Egelhoff, Jr., Phys. Rev. Lett. **59**, 559 (1987).

[9] S. Y. Tong, H. Huang, and Hua Li, in *Advances in Surface and Thin Film Diffraction,* edited by T. C. Huang, P. I. Cohen, and D. J. Eaglesham, MRS Symposia Proceedings No. 208 (Materials Research Society, Pittsburgh, 1991), p. 13.

[10] S. Y. Tong, Hua Li, and H. Huang (to be published).

[11] J. J. Barton and L. J. Terminello, in *The Structure of Surfaces-III,* edited by S. Y. Tong, M. A. Van Hove, X. Xie, and K. Takayanagi (Springer, Berlin, 1991).

[12] S. Thevuthasan, G. S. Herman, A. P. Kaduwela, R. S. Saiki, Y. J. Kim, and C. S. Fadley, Phys. Rev. Lett. **67**, 469 (1991).

[13] D. K. Saldin, G. R. Harp, B. L. Chen, and B. P. Tonner, Phys. Rev. B **44**, 2480 (1991).

[14] P. Bedrossian, R. D. Meade, K. Mortensen, D. M. Chen, J. A. Golovchenko, and D. Vanderbilt, Phys. Rev. Lett. **63**, 2357 (1989).

[15] I.-W. Lyo, E. Kaxiras, and Ph. Avouris, Phys. Rev. Lett. **53**, 1261 (1989).

[16] L. Headrich, I. K. Robinson, E. Vlieg, and L. G. Feldman, Phys. Rev. Lett. **63**, 1253 (1989).

[17] E. Kaxiras, K. C. Pandey, F. J. Himpsel, and R. M. Tromp, Phys. Rev. B **41**, 1262 (1990).

[18] H. Huang, S. Y. Tong, J. Quinn, and F. Jona, Phys. Rev. B **41**, 3276 (1990).

[19] S. Y. Tong, C. H. Li, and A. R. Lubinsky, Phys. Rev. Lett. **39**, 498 (1977).

[20] C. H. Li, A. R. Lubinsky, and S. Y. Tong, Phys. Rev. B **17**, 3128 (1978).

[21] J. J. Rehr and R. C. Albers, Phys. Rev. B **41**, 8139 (1990).

[22] J. J. Barton and D. A. Shirley, Phys. Rev. B **32**, 1906 (1985).

[23] S. Y. Tong and C. H. Li, in *Critical Reviews in Solid State and Materials Sciences,* edited by D. E. Schuele and R. W. Hoffman (CRC, Cleveland, 1981), Vol. 10, p. 209.

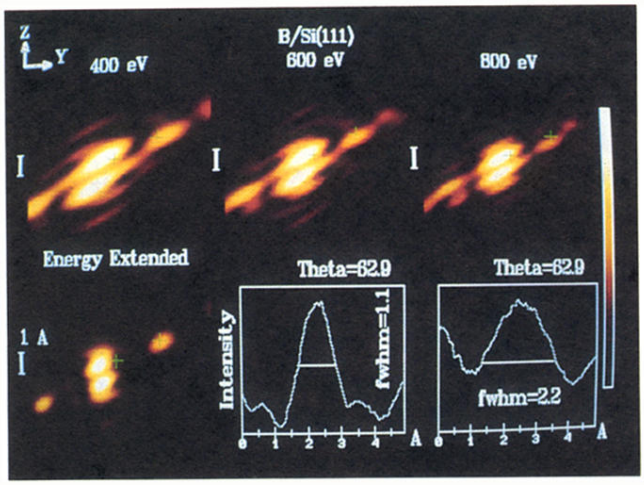

FIG. 2. Small-window $\theta_c = 45°$ image of Si(3) in the y-z plane; top left, center, and right show single-energy reconstructions; bottom left shows 3-energy combined reconstruction; crosses mark origin and correct atomic position. Bottom center and right show, respectively, intensity variation along the B-Si(3) internuclear direction for 3-energy combined and 400-eV reconstructions. The origin is at the B atomic center.

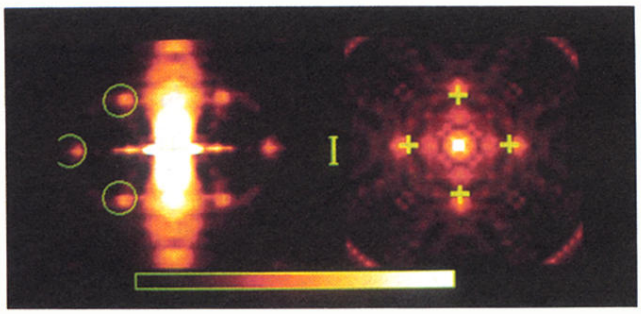

FIG. 3. Left: Full-window $\theta_e = 90°$ image of Ni atoms (inside circles) in a plane normal to the surface, the cross marks the Cu emitter. The $+\hat{z}$ direction points from left to right and the twin images are mirrored on the right half. The energy range is 60–681 eV. Right: Plane parallel to the surface, crosses mark the correct atomic positions. The vertical bar indicates 1 Å.

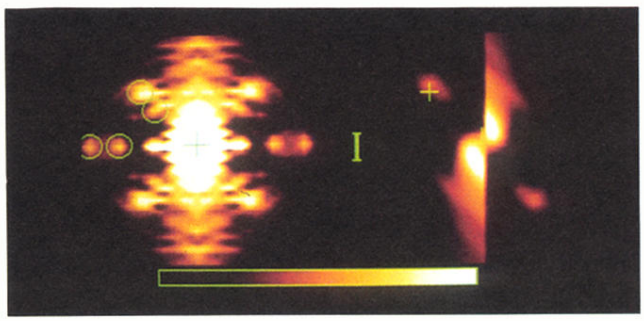

FIG. 4. Left: Full-window $\theta_c = 90°$ Ni images using nine energies in the 60–286 eV range. Other conditions are the same as those in Fig. 3, left. The Ni images are split (marked by circles). Right: Small-window $\theta_c = 45°$ image of nearest-neighbor Ni atom. Crosses mark the origin (emitter) and correct Ni atomic position. The vertical bar indicates 1 Å.